Front. Mater. Sci. 2018, 12(3): 225–238
https://doi.org/10.1007/s11706-018-0428-x

RESEARCH ARTICLE

All-conjugated amphiphilic diblock copolymers for improving morphology and thermal stability of polymer/nanocrystals hybrid solar cells

Zhenrong JIA[1,2*], Xuefeng XIA[1*], Xiaofeng WANG (✉)[1], Tengyi WANG[1], Guiying XU[1], Bei LIU[1], Jitong ZHOU[1], and Fan LI (✉)[1]

1 Department of Materials Science and Engineering, Nanchang University, 999 Xuefu Avenue, Nanchang 330031, China
2 Beijing National Laboratory for Molecular Sciences, CAS Key Laboratory of Organic Solids, Institute of Chemistry, Chinese Academy of Sciences, Beijing 100190, China

ABSTRACT: Herein, the ability to optimize the morphology and photovoltaic performance of poly(3-hexylthiophene) (P3HT)/ZnO hybrid bulk-heterojunction solar cells via introducing all-conjugated amphiphilic P3HT-based block copolymer (BCP), poly(3-hexylthiophene)-*block*-poly(3-triethylene glycol-thiophene) (P3HT-*b*-P3TEGT), as polymeric additives is demonstrated. The results show that the addition of P3HT-*b*-P3TEGT additives can effectively improve the compatibility between P3HT and ZnO nanocrystals, increase the crystalline and ordered packing of P3HT chains, and form optimized hybrid nanomorphology with stable and intimate hybrid interface. The improvement is ascribed to the P3HT-*b*-P3TEGT at the P3HT/ZnO interface that has strong coordination interactions between the TEG side chains and the polar surface of ZnO nanoparticles. All of these are favor of the efficient exciton dissociation, charge separation and transport, thereby, contributing to the improvement of the efficiency and thermal stability of solar cells. These observations indicate that introducing all-conjugated amphiphilic BCP additives can be a promising and effective protocol for high-performance hybrid solar cells.

KEYWORDS: hybrid solar cell; P3HT; ZnO; all-conjugated amphiphilic block copolymer; additive

Contents

Received April 17, 2018; accepted May 23, 2018

E-mails: wxfeng@ncu.edu.cn (X.W.), lfan@ncu.edu.cn (F.L.)

* Z.J. and X.X. contributed equally to this work.

1 Introduction

The main interest in organic–inorganic hybrid bulk-heterojunction (BHJ) solar cells stems from their combined advantages of the conjugated polymers donor and inorganic semiconducting nanocrystals acceptor [1–2].

The conjugated polymers deliver the light-weight, mechanical flexibility, low fabrication cost and good opto-electronic characteristics and inorganic nanocrystals offer the tunable bandgap, low synthetic cost and high electron mobility [3–7]. Contributed to these advantages, hybrid solar cells (HSCs) become a viable candidate of photovoltaic applications [8–10]. However, the power conversion efficiencies (PCEs) of HSCs are relatively poor in comparison with those of the fullerene or nonfullerene polymer solar cells (PSCs) [11–13], due to the macrophase separation and incompatibility organic/inorganic hybrid interfaces. Therefore, it is a critical issue to overcome the aggregation of nanocrystals and achieve a bi-continuous interpenetrating nanostructured hybrid BHJ with well-defined hybrid interfaces. Such favorable blending morphology can match the size of the exciton diffusion length (10–20 nm) and facilitate charge separation and transport of HSCs.

For these purposes, many approaches, such as ligand-exchange [14], grafting polymers onto nanocrystals [15], *in-situ* formation of polymer–nanocrystals hybrid systems [16–18] have been exploited to achieve the favorable hybrid BHJ. However, above mentioned methods still suffer from other problems: slow and incomplete ligand exchange process, complicated and subtle grafting route, and uncontrolled hybrid nanomorphologies via *in-situ* methods [19]. Thus, much attention should be paid to develop a simple and effective strategy to optimize nanoscale phase separation and enhance the polymer/inorganic nanocrystals interfacial interactions.

Recently, the utilization of poly(3-hexylthiophene) (P3HT)-based all-conjugated block copolymers (BCPs) as nanostructuring additives in P3HT-based organic photovoltaics (OPVs) has attracted increasing interests [20–22]. These P3HT-based BCPs encompass the superior opto-electronic property of P3HT backbone and the fascinating self-assembly ability to form stable nanoscaled phase-separated D/A interpenetrating networks. Moreover, it has been demonstrated that such easy method can not only optimize the active layer nanoscale morphology but also promote the morphological stability [22]. At the same time, it has been reported that the organization and dispersion of inorganic nanocrystals can be well-controlled induced by the self-assembly behavior of amphiphilic BCPs originating from the chemically distinct polymeric segments [23–24].

Motivated by the aforementioned specific merits of all-conjugated BCPs and amphiphilic BCPs, we synthesized an all-conjugated amphiphilic P3HT-based BCP, poly(3-hexylthiophene)-*block*-poly(3-triethylene glycol-thiophene) (P3HT-*b*-P3TEGT), and introduced into the P3HT and ZnO nanoparticles (NPs) hybrid system as the polymeric additive to optimize BHJ solar cells. The main motivations to choose P3HT-*b*-P3TEGT as nanostructuring additives in P3HT/ZnO HSCs are as follows: (i) TEG side chains in the polar hydrophilic P3TEGT block have strong affinity to nanocrystals and can act as "stabilizers" to avoid the conglomeration of ZnO NPs and passivate their surface defects [25]; (ii) The BCP acts as a "linker" at P3HT/ZnO interface to enhance the miscibility and expand the D/A interfacial areas because two blocks of BCPs have compatibilities with donor and acceptor, respectively; (iii) P3HT-*b*-P3TEGT has been shown to generate various highly ordered nanostructures resulting from the interplay between self-assembly and phase separation, which allows for facilitating morphology optimization and interchain stacking of the P3HT [26–27].

In this work, we investigated the influences of different amount of P3HT-*b*-P3TEGT BCPs on the morphology, photovoltaic properties of P3HT/ZnO hybrid BHJ in detail, as well as the thermal stability of the corresponding devices. As expected, the introduction of appropriate amount of P3HT-*b*-P3TEGT additives can effectively control P3HT/ZnO blend morphology, strengthen the hybrid interface interaction, and enhance the crystallinity of P3HT. As a result, the enhanced efficiency and stability of device were acquired because of the improved exciton dissociation, charge separation and transport, and more stable hybrid morphology. The significance of this work is to demonstrate a simple and effective approach to improve the morphology and photovoltaic performance of hybrid BHJ solar cells. The detailed experimental process is shown in the part of "Supplementary information".

2 Results and discussion

Figure 1(a) shows the device structure of the HSCs and the corresponding chemical structure of each component in the active layer. P3HT-*b*-P3TEGT was prepared via a nickel-catalyzed quasi-living Grignard metathesis (GRIM) polymerization according to Refs. [26–27] and the detailed synthetic route and experimental details were depicted in Scheme S1 and the part of "Supplementary information". The chemical structures of obtained monomers and P3HT-*b*-P3TEGT diblock copolymer were characterized by

proton nuclear magnetic resonance (^{1}H NMR) (Figs. S1 and S2), which proved that the P3HT-*b*-P3TEGT had been successfully synthesized. As shown in Fig. S3, the polystyrene-equivalent molecular weight of P3HT-*b*-P3TEGT was M_n = 11800 g/mol and PDI was 1.55 estimated by gel permeation chromatography (GPC). To explore the thermal properties of P3HT-*b*-P3TEGT, thermogravimetry (TGA) and differential scanning calorimetry (DSC) analysis were implemented. P3HT-*b*-P3TEGT exhibited excellent thermal stability and almost lost no weight at temperature as high as 421°C (Fig. S4). The melting temperature (T_m) of P3HT-*b*-P3TEGT was 175°C (Fig. S5). Such thermal stability is good enough for the application in HSCs. The UV-vis absorption properties of P3HT-*b*-P3TEGT both in 1,2-dichlorobenzene solution and as the thin solid film were also studied (Fig. S6). An obvious red shift of 58 nm could be observed for the absorption from solution to thin film due to the molecular aggregation and the appearance of the absorption peak at 605 nm for the P3HT-*b*-P3TEGT thin film could be assigned to the π–π stacking among the P3HT blocks [28–29]. The optical bandgap was estimated to be 1.93 eV from the absorption edge, which was in accordance with the literature [26]. The highest occupied molecular orbital (HOMO) and lowest unoccupied molecular orbital (LUMO) energy levels of P3HT-*b*-P3TEGT were obtained by cyclic voltammetry (CV) (Fig. S7). The HOMO and LUMO levels were estimated to be −5.13 and −3.19 eV, respectively and the electrochemical bandgap was calculated to be 1.94 eV, which agreed with the result of UV-vis absorption. It was clear that the energy level of P3HT-*b*-P3TEGT lied between the energy levels of P3HT and ZnO (Fig. 1(b)), which would facilitate the electron transport from P3HT to ZnO NPs. The basic properties of P3HT-*b*-P3TEGT thin film were summarized in Table 1. ZnO NPs used in the experiment were synthesized according to the previous report [30]. From the TEM images (Fig. S8), it could be seen that the average particle size of the as-synthesized ZnO NPs was about 5 nm and ZnO NPs showed high crystallinity.

To reveal the influence of P3HT-*b*-P3TEGT doping on the physical conformation and crystallinity of the P3HT/ZnO blend films, UV-vis absorption spectra were performed. Normalized optical absorbance spectra of P3HT/ZnO thin films with different amounts of P3HT-*b*-P3TEGT were shown in Fig. 2(a). It was observed that there was no apparent difference in the absorption spectra of the P3HT/ZnO film and the P3HT/ZnO/P3HT-*b*-P3TEGT ternary blend films. All samples exhibited three absorption peaks at 521, 560 and 605 nm, which was the typical absorption characteristic of P3HT [28–29]. The intensity of a shoulder peak at 605 nm obviously increased upon adding P3HT-*b*-

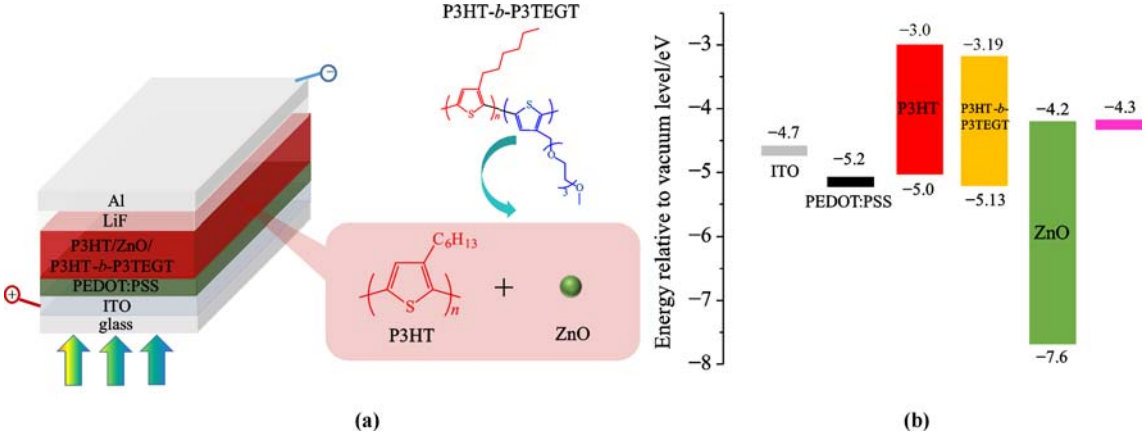

Fig. 1 **(a)** Schematic illustration of the device structure and the corresponding chemical structures of components in the active layer of HSCs. **(b)** The energy band diagram of the HSCs based on P3HT/ZnO/P3HT-*b*-P3TEGT.

Table 1 Basic properties of the P3HT-*b*-P3TEGT film

Polymer	M_n [a)]/(g·mol^{-1})	PDI [a)]	T_d [b)]/°C	λ_{max}/nm	λ_{onset}/nm	E_g^{opt} [c)]/eV	HOMO [d)]/eV	LUMO [e)]/eV	E_g^{ec} [f)]/eV
P3HT-*b*-P3TEGT	7700	2.39	421	511	644	1.93	−5.13	−3.19	1.94

a) Determined by GPC using polystyrene standards and THF as the eluent.
b) 5% weight-loss temperature under N_2.
c) Calculated from the absorption edges of the polymer film, $E_g^{opt} = 1240/\lambda_{onset}$.
d) HOMO was acquired according to the empirical formulae HOMO = $-(E_{ox} + 4.4)$ eV.
e) LUMO was acquired according to the empirical formulae LUMO = $-(E_{red} + 4.4)$ eV.
f) E_g^{ec} was calculated from E_g^{ec} = LUMO − HOMO.

P3TEGT, especially for loading 5% of P3HT-*b*-P3TEGT. As we known, the appearance of the shoulder peak at 605 nm was associated with the strong intermolecular interaction of π–π stacking of P3HT chains [31]. Thus, the increased absorption intensity at 605 nm with the addition of P3HT-*b*-P3TEGT indicated that the introduction of a small amount of P3HT-*b*-P3TEGT could promote the crystallization and ordering packing of P3HT chains.

X-ray diffraction (XRD) experiments were aimed to obtain deeper insight into the structural order of P3HT doped by P3HT-*b*-P3TEGT (Fig. 2(b)). The diffraction peak at 5.4° arose from the (100) plane of P3HT, corresponding to the lamellar packing of P3HT chains [32]. And the peaks in the range of 20°–60° were originating from the crystalline ZnO. The addition of P3HT-*b*-P3TEGT did not affect ZnO crystal structures because the diffraction peaks of ZnO in P3HT/ZnO/P3HT-*b*-P3TEGT ternary blend films were almost unchanged compared with those of the P3HT/ZnO film (inset of Fig. 2(b)). However, it was noteworthy that upon adding P3HT-*b*-P3TEGT, the intensity and full width at half maximum (FWHM) of the P3HT (100) diffraction peak became stronger and smaller, respectively, especially for 5% loading of P3HT-*b*-P3TEGT (Fig. S9). The FWHM values of the P3HT (100) peak were 0.94°, 0.92°, 0.80° and 0.85° for P3HT/ZnO and P3HT/ZnO blended with 1%, 5%, 10% P3HT-*b*-P3TEGT, respectively. The result indicated that P3HT-*b*-P3TEGT additives could increase the crystallization of the P3HT domains, which was consistent with the UV-vis absorption analysis. The improved crystallization and ordering packing of P3HT will facilitate the charge transport, thus, increasing the photovoltaic performance. Here, we also noted that the crystalline and ordered packing of P3HT in the ternary films blended with 10% of P3HT-*b*-P3TEGT decreased, which might be related to the disturbed molecular arrangement of P3HT/ZnO due to the high P3HT-*b*-P3TEGT content [33].

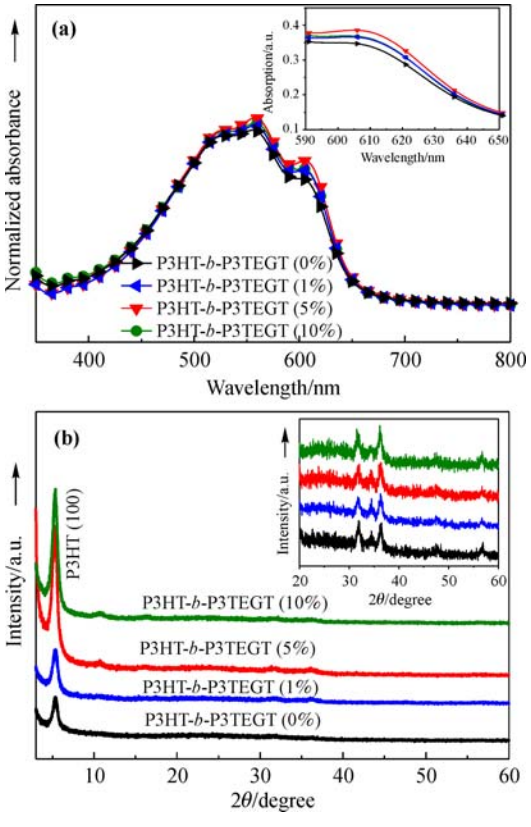

Fig. 2 **(a)** UV-vis absorption spectra of P3HT/ZnO films blended with different amounts of P3HT-*b*-P3TEGT. **(b)** XRD patterns of P3HT/ZnO films blended with different amounts of P3HT-*b*-P3TEGT (inset: XRD patterns in the range of 20°–60°).

Photoluminescence (PL) is related to the recombination of photogenerated excitons and it can be used to evaluate the exciton dissociation followed by charge transfer from the electron donor to the electron acceptor at the D/A interface [34]. Therefore, PL spectra were measured to investigate the charge transfer at the hybrid interface in the P3HT/ZnO/P3HT-*b*-P3TEGT blend films. Figures 3(a) and 3(b) showed the steady-state and time-resolved PL spectra of P3HT/ZnO films blended with different amounts of P3HT-*b*-P3TEGT, respectively. It was noted that compared to the P3HT/ZnO film, stronger and faster PL delay was observed with the addition of P3HT-*b*-P3TEGT into the P3HT/ZnO film, especially when the P3HT-*b*-P3TEGT weight fraction was 5%. The results showed that more efficient charge separation and transfer occurred at the P3HT/ZnO hybrid interface with the introduction of P3HT-*b*-P3TEGT additives. In our experiment, the oxygen atoms of TEG side chains in the P3TEGT block of P3HT-*b*-P3TEGT amphiphilic BCPs could complex metal ions and might affect the surface state of ZnO NPs. To reveal the effect of P3HT-*b*-P3TEGT on the surface defects of ZnO NPs, we performed another PL measurement using the 325 nm as the excitation wavelength, shown in Fig. S10. Generally speaking, there are two PL emission bands in wurtzite ZnO: band-edge UV emission and defect-related visible emission [35]. It could be found that the intensity of the peak at the UV region (379 nm) relative to the peak at the visible region increased upon introducing P3HT-*b*-P3TEGT in P3HT/ZnO, implying that the surface defects of ZnO NPs could be passivated via introducing P3HT-*b*-P3TEGT [36]. Based on the above observations, the PL

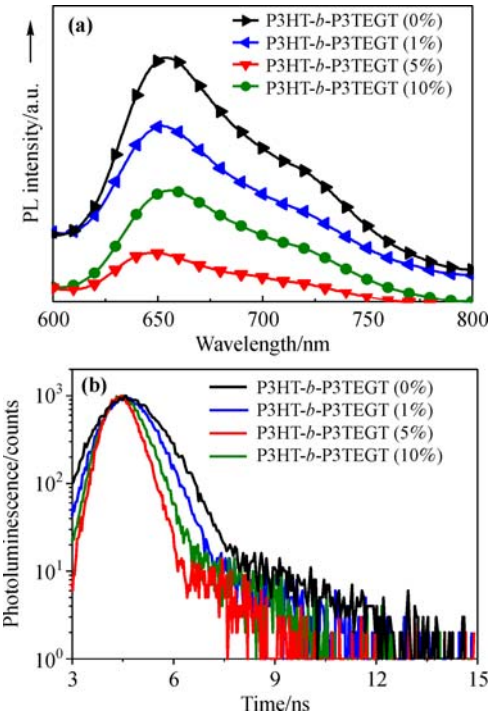

Fig. 3 **(a)** Steady-state PL spectra of P3HT/ZnO films blended with different amounts of P3HT-*b*-P3TEGT (λ_{ex} = 460 nm). **(b)** Time-resolved PL decay spectra of P3HT/ZnO films blended with different amounts of P3HT-*b*-P3TEGT (λ_{ex} = 460 nm).

quenching in the P3HT/ZnO/P3HT-*b*-P3TEGT films could be attributed to the formation of fine nanoscale phase-separated morphology for efficient exciton dissociation (*vide infra*) and improved interfacial interaction between P3HT and ZnO for charge transfer due to the presence of P3HT-*b*-P3TEGT.

The morphology of the hybrid BHJ is an important factor affecting photovoltaic device performance in HSCs. To examine the effect of incorporating P3HT-*b*-P3TEGT on the film morphology of the P3HT/ZnO blend film, transmission electron microscopy (TEM) and tapping-mode atomic force microscopy (AFM) measurements were conducted on the active layer films (Figs. 4 and S11). For TEM images, the P3HT/ZnO or P3HT/ZnO/P3HT-*b*-P3TEGT blend films were spin-coated on PEDOT:PSS coated ITO glass and dipped into a Petri dish containing deionized (DI) water. Then the floating films were placed on carbon coated copper grid. As shown in Fig. 4, the P3HT/ZnO showed serious macroscopic phase segregation, which likely resulted in the poor photovoltaic properties. Encouragingly, when the P3HT-*b*-P3TEGT BCP was introduced, the better dispersion of ZnO NPs could be observed, especially in the case of adding 5% P3HT-*b*-P3TEGT.

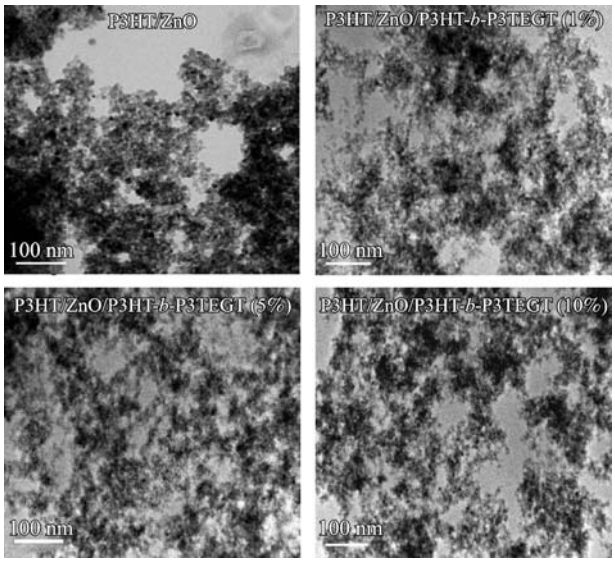

Fig. 4 TEM images of P3HT/ZnO films blended with different amounts of P3HT-*b*-P3TEGT.

The same change tendency could also observed in the AFM images (Fig. S11). For the P3HT/ZnO, we could observe many large nanoparticle aggregates in the top of film, exhibiting a rough surface with a root-mean-square (RMS) roughness of 24.1 nm. With the incorporation of P3HT-*b*-P3TEGT, the surface of ternary thin films became smoother and more uniform. This smoother surface can provide good contact between active layer and electrodes, with more efficient charge transport [25]. Specially, the P3HT/ZnO films blended with 5% P3HT-*b*-P3TEGT showed a RMS of only 6.77 nm. It was reasonable to conclude that the interactions between the P3TEGT block and the ZnO NPs could improve the compatibility of polymer and ZnO NPs and effectively suppress the ZnO NPs aggregation, forming better nano-morphology of hybrid BHJ for a higher exciton dissociation and charge transport efficiency.

According to the above results, we could infer that thanks to the strong coordination interactions between the hydrophilic P3TEGT block and polar surface of ZnO NPs and the similarities in the chemical structure of P3HT-*b*-P3TEGT to the P3HT/ZnO hybrid, P3HT-*b*-P3TEGT would preferentially reside at the interfaces between P3HT and ZnO NPs with the P3HT block interacting with the P3HT homopolymer and the P3TEGT block interacting with the ZnO NPs (Scheme 1). As a result, P3HT-*b*-P3TEGT could act as a “linker” between P3HT and ZnO to improve the miscibility of D/A interface and enhance the ordered packing of P3HT. Eventually, optimized and stabilized nanoscale morphology of active

layers could be realized. Therefore, improved device performance, as well as better device thermal stability, could be expected.

To investigate the influences of P3HT-*b*-P3TEGT additive on the photovoltaic performance, hybrid BHJ solar cells with the device structure of ITO/PEDOT:PSS/photoactive layer/LiF/Al were fabricated. The current density–voltage (*J*–*V*) characteristics were shown in Fig. 5 and the relevant photovoltaic parameters were summarized in Table 2. The P3HT/ZnO reference photovoltaic device exhibited a PCE of 0.34% with a J_{sc} of 1.44 mA/cm^2, a V_{oc} of 0.47 V and a *FF* of 0.50. When the P3HT-*b*-P3TEGT was added, the performance of all photovoltaic devices outperformed that of the P3HT/ZnO control device. The highest efficiency of 0.81% was achieved for the photovoltaic device blended with 5% P3HT-*b*-P3TEGT, corresponding to 2.4 times relative to the control device. Further observing the photovoltaic parameters, we could find that the significant increase in PCE was mainly attributed to the obvious improvement in the J_{sc} and *FF* along with slightly improved V_{oc}. According to literature report, the V_{oc} is mainly affected by the energy different between the HOMO level of the electron donor and the LUMO level of the electron acceptor, as well as the work function of electrodes. The slight increase of V_{oc} in our cases might be the possible interaction between TEG side chains of P3HT-*b*-P3TEGT and electrodes [37]. The enhancement of J_{sc} could be mainly attributed to the enhanced crystallinity of P3HT polymer chains and the more intimate donor/acceptor interface, resulting in efficient charge transfer and transport. The increase of *FF* could be attributed to the better phase separation with proper domain size equal to the exciton diffusion length (~10 nm) leading to the more efficient exciton diffusion and dissociation [38]. Another reason was that the incorporation of P3HT-*b*-P3TEGT could decrease RMS roughness of the blend films. Such smoother surface would provide fewer defects and better contact with electrode, which could decrease charge loss and contact resistance with the electrode for more efficient charge transport

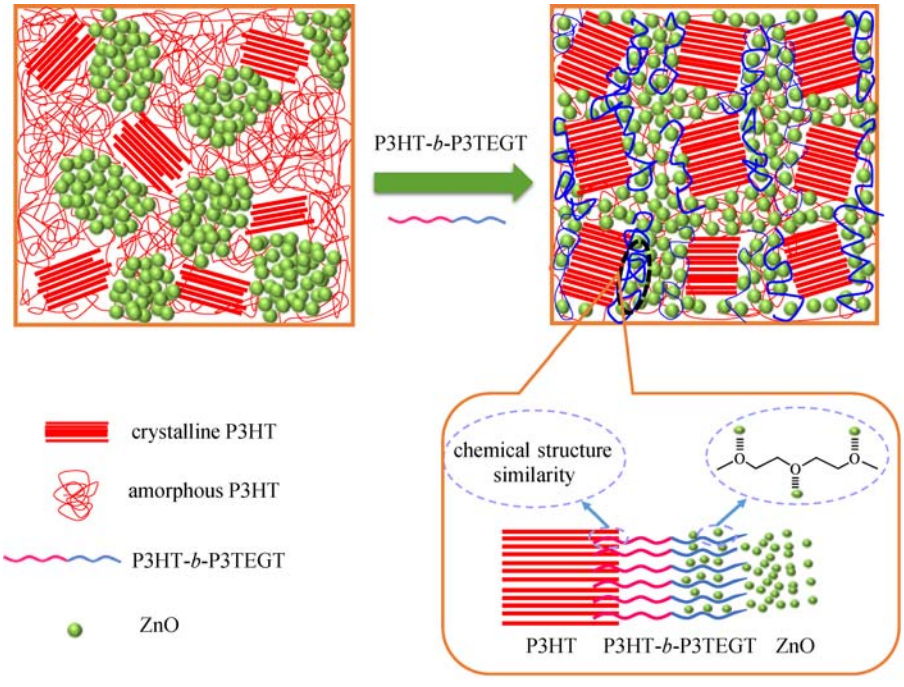

Scheme 1 Illustrations of the morphologies of active layers in the BHJ solar cells with (right) and without (left) P3HT-*b*-P3TEGT.

Table 2 Characteristic current–voltage parameters of HSCs based on P3HT/ZnO with different amounts of P3HT-*b*-P3TEGT BCPs

Device	J_{sc}/(mA·cm^{-2})	V_{oc}/V	*FF*	PCE [Avg] [a)]/%
w/o P3HT-*b*-P3TEGT	1.44	0.47	0.50	0.34 [0.32]
P3HT-*b*-P3TEGT (1%)	1.82	0.53	0.52	0.50 [0.47]
P3HT-*b*-P3TEGT (5%)	2.60	0.52	0.60	0.81 [0.79]
P3HT-*b*-P3TEGT (10%)	2.37	0.52	0.54	0.67 [0.64]

a) Data are averaged over at least six devices.

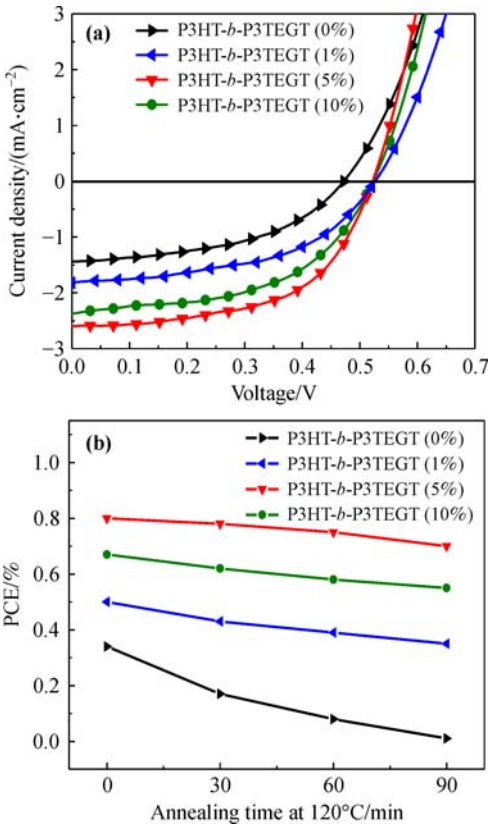

Fig. 5 **(a)** Current–voltage characteristics of photovoltaic cells based on P3HT/ZnO with different amounts of P3HT-*b*-P3TEGT hybrid films. **(b)** PCE of P3HT/ZnO/P3HT-*b*-P3TEGT BHJ HSC devices with different amounts of P3HT-*b*-P3TEGT diblock copolymer as a function of annealing time at 120°C.

[22,39–40]. However, a higher loading of P3HT-*b*-P3TEGT (10%) would lead to the decrease of PCE. We attributed the reduced PCE to the less conductive P3TEGT blocks in the P3HT-*b*-P3TEGT, which would hinder charge transport, thereby, degrading the device performance.

To investigate the influence of P3HT-*b*-P3TEGT additives on the thermal stability of the photovoltaic devices, the completed devices were fabricated and subsequently annealed at 120°C. The PCEs of HSCs based on P3HT/ZnO blended with different amounts of P3HT-*b*-P3TEGT were recorded as a function of annealing time (Fig. 5(b)). Relative to the P3HT/ZnO device, all P3HT/ZnO/P3HT-*b*-P3TEGT devices exhibited an improvement in their thermal stability. This indicated that addition of P3HT-*b*-P3TEGT in P3HT/ZnO could endow the device with better thermal stability. Optical microscopy images of the active layers could also be applied to gain direct insight into the origin of the thermal stability of devices (Fig. 6). For the P3HT/ZnO thin film, thermal treatment at 120°C for 10 min induced the formation of some ZnO NPs aggregates. Further prolonging the annealing time, the large-scale ZnO NPs aggregates appeared, which would reduce the interfacial area and charge separation and transport, deteriorating the device performance. On the contrary, the ZnO aggregations could be effectively suppressed upon adding P3HT-*b*-P3TEGT additives, indicating that the selective miscibility of the P3TEGT block with ZnO caused the surface compatibilizing effect, inhibiting the severe aggregation of ZnO NPs and improving the device stability.

3 Conclusions

In summary, we demonstrated an effective approach for optimizing the morphology and photovoltaic performance of P3HT/ZnO HSCs using the all-conjugated amphiphilic

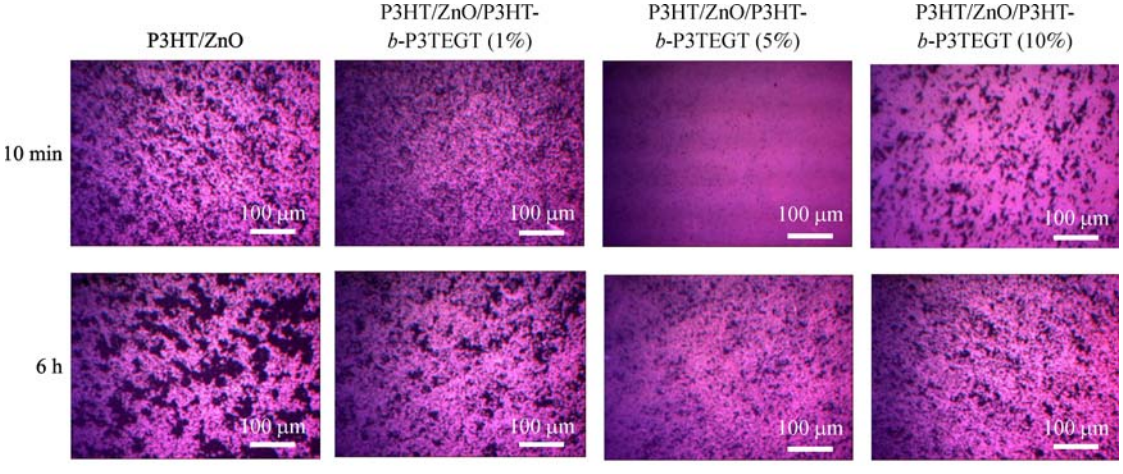

Fig. 6 Optical microscopy images of P3HT/ZnO hybrid films blended with different amount of P3HT-*b*-P3TEGT under 120°C for 10 min and 6 h.

P3HT-based diblock copolymers P3HT-*b*-P3TEGT as polymeric additives. Moreover, the presence of P3HT-*b*-P3TEGT could lead to the increased crystallization and ordered packing of P3HT. Consequently, a favored active layer morphology have been obtained and the photovoltaic performance of P3HT/ZnO HSCs was improved, which mainly contributed to the enhancement of J_{sc}. Furthermore, the incorporation of P3HT-*b*-P3TEGT BCPs could also suppress the macrophase separation of hybrid active layer during thermal annealing. Overall, these results proved that the P3HT-*b*-P3TEGT played a critical role in forming an optimized morphology in the P3HT/ZnO blend films, resulting in high-performance and thermal stable hybrid photovoltaic devices.

Disclosure of potential conflicts of interests The authors declare no competing financial interest.

Acknowledgements This work was supported by the National Natural Science Foundation of China (Grant Nos. 61464006 and 61664006) and the Natural Science Foundation of Jiangxi Province, China (20171ACB21010). F.L. acknowledges the support from the Jiangxi Province Young Scientist Project (20142BCB23002).

References

[1] Huynh W U, Dittmer J J, Alivisatos A P. Hybrid nanorod-polymer solar cells. Science, 2002, 295(5564): 2425–2427

[2] Gao F, Ren S, Wang J. The renaissance of hybrid solar cells: progresses, challenges, and perspectives. Energy & Environmental Science, 2013, 6(7): 2020–2040

[3] Sun Y, Liu Z, Yuan J, et al. Polymer selection toward efficient polymer/PbSe planar heterojunction hybrid solar cells. Organic Electronics, 2015, 24: 263–271

[4] Yue W, Wei F, Li Y, et al. Hierarchical $CuInS_2$ synthesized with the induction of histidine for polymer/$CuInS_2$ solar cells. Materials Science in Semiconductor Processing, 2018, 76: 14–24

[5] Giansante C, Mastria R, Lerario G, et al. Molecular-level switching of polymer/nanocrystal non-covalent interactions and application in hybrid solar cells. Advanced Functional Materials, 2015, 25(1): 111–119

[6] Li F, Shi Y, Yuan K, et al. Fine dispersion and self-assembly of ZnO nanoparticles driven by P3HT-*b*-PEO diblocks for improvement of hybrid solar cells performance. New Journal of Chemistry, 2013, 37(1): 195–203

[7] Liu Z, Sun Y, Yuan J, et al. High-efficiency hybrid solar cells based on polymer/PbS_xSe_{1-x} nanocrystals benefiting from vertical phase segregation. Advanced Materials, 2013, 25(40): 5772–5778

[8] Chen Z, Zhang H, Du X, et al. From planar-herterojunction to n-i structure: An efficient strategy to improve short-circuit current and power conversion efficiency of aqueous-solution-processed hybrid solar cells. Energy & Environmental Science, 2013, 6(5): 1597–1603

[9] Im S H, Lim C S, Chang J A, et al. Toward interaction of sensitizer and functional moieties in hole-transporting materials for efficient semiconductor-sensitized solar cells. Nano Letters, 2011, 11(11): 4789–4793

[10] Chang J A, Im S H, Lee Y H, et al. Panchromatic photon-harvesting by hole-conducting materials in inorganic–organic heterojunction sensitized-solar cell through the formation of nanostructured electron channels. Nano Letters, 2012, 12(4): 1863–1867

[11] Vohra V, Kawashima K, Kakara T, et al. Efficient inverted polymer solar cells employing favourable molecular orientation. Nature Photonics, 2015, 9(6): 403–408

[12] Chen Y, Ye P, Zhu Z G, et al. Achieving high-performance ternary organic solar cells through tuning acceptor alloy. Advanced Materials, 2017, 29(6): 1603154

[13] Zhao W, Li S, Yao H, et al. Molecular optimization enables over 13% efficiency in organic solar cells. Journal of the American Chemical Society, 2017, 139(21): 7148–7151

[14] Giansante C, Infante I, Fabiano E, et al. "Darker-than-black" PbS quantum dots: enhancing optical absorption of colloidal semiconductor nanocrystals via short conjugated ligands. Journal of the American Chemical Society, 2015, 137(5): 1875–1886

[15] Zhao L, Pang X, Adhikary R, et al. Semiconductor anisotropic nanocomposites obtained by directly coupling conjugated polymers with quantum rods. Angewandte Chemie International Edition, 2011, 50(17): 3958–3962

[16] Jaimes W, Alvarado-Tenorio G, Martínez-Alonso C, et al. Effect of CdS nanoparticle content on the *in-situ* polymerization of 3-hexylthiophene-2,5-diyl and the application of P3HT-CdS products in hybrid solar cells. Materials Science in Semiconductor Processing, 2015, 37: 259–265

[17] Lewis E A, McNaughter P D, Yin Z, et al. *In situ* synthesis of PbS nanocrystals in polymer thin films from lead(II) xanthate and dithiocarbamate complexes: evidence for size and morphology control. Chemistry of Materials, 2015, 27(6): 2127–2136

[18] MacLachlan A J, Rath T, Cappel U B, et al. Polymer/nanocrystal hybrid solar cells: influence of molecular precursor design on film nanomorphology, charge generation and device performance. Advanced Functional Materials, 2015, 25(3): 409–420

[19] Zhao L, Lin Z. Crafting semiconductor organic–inorganic nanocomposites via placing conjugated polymers in intimate contact with nanocrystals for hybrid solar cells. Advanced Materials, 2012, 24(32): 4353–4368

[20] Sun Y, Pitliya P, Liu C, et al. Block copolymer compatibilized

polymer: fullerene blend morphology and properties. Polymer, 2017, 113: 135–146

[21] Mitchell V D, Gann E, Huettner S, et al. Morphological and device evaluation of an amphiphilic block copolymer for organic photovoltaic applications. Macromolecules, 2017, 50(13): 4942–4951

[22] Zhu M, Kim H, Jang Y J, et al. Toward high efficiency organic photovoltaic devices with enhanced thermal stability utilizing P3HT-*b*-P3PHT block copolymer additives. Journal of Materials Chemistry A: Materials for Energy and Sustainability, 2016, 4 (47): 18432–18443

[23] Li J H, Li Y, Xu J T, et al. Self-assembled amphiphilic block copolymers/CdTe nanocrystals for efficient aqueous-processed hybrid solar cells. ACS Applied Materials & Interfaces, 2017, 9 (21): 17942–17948

[24] Yao S, Chen Z, Li F, et al. High-efficiency aqueous-solution-processed hybrid solar cells based on P3HT dots and CdTe nanocrystals. ACS Applied Materials & Interfaces, 2015, 7(13): 7146–7152

[25] Shi Y, Li F, Chen Y. Controlling morphology and improving the photovoltaic performances of P3HT/ZnO hybrid solar cells via P3HT-*b*-PEO as an interfacial compatibilizer. New Journal of Chemistry, 2013, 37(1): 236–244

[26] Lee E, Hammer B, Kim J K, et al. Hierarchical helical assembly of conjugated poly(3-hexylthiophene)-*block*-poly(3-triethylene glycol thiophene) diblock copolymers. Journal of the American Chemical Society, 2011, 133(27): 10390–10393

[27] Song I Y, Kim J, Im M J, et al. Synthesis and self-assembly of thiophene-based all-conjugated amphiphilic diblock copolymers with a narrow molecular weight distribution. Macromolecules, 2012, 45(12): 5058–5068

[28] Yamamoto T, Komarudin D, Arai M, et al. Extensive studies on π-stacking of poly(3-alkylthiophene-2,5-diyl)s and poly(4-alkylthiazole-2,5-diyl)s by optical spectroscopy, NMR analysis, light scattering analysis, and X-ray crystallography. Journal of the American Chemical Society, 1998, 120(9): 2047–2058

[29] Mena-Osteritz E, Meyer A, Langeveld-Voss B M W, et al. Two-dimensional crystals of poly(3-alkyl-thiophene)s: direct visualization of polymer folds in submolecular resolution. Angewandte Chemie International Edition, 2000, 112(15): 2791–2796

[30] Beek W J E, Wienk M M, Kemerink M, et al. Hybrid zinc oxide conjugated polymer bulk heterojunction solar cells. The Journal of Physical Chemistry B, 2005, 109(19): 9505–9516

[31] Jia Z, Wei Y, Wang X, et al. Improvement of morphology and performance of P3HT/ZnO hybrid solar cells induced by liquid crystal molecules. Chemical Physics Letters, 2016, 661: 119–124

[32] Prosa T J, Winokur M J, Moulton J, et al. X-ray structural studies of poly(3-alkylthiophenes): an example of an inverse comb. Macromolecules, 1992, 25(17): 4364–4372

[33] Hu Z, Tang S, Ahlvers A, et al. Near-infrared photoresponse sensitization of solvent additive processed poly(3-hexylthiophene)/fullerene solar cells by a low band gap polymer. Applied Physics Letters, 2012, 101(5): 053308

[34] Salim T, Lee H W, Wong L H, et al. Semiconducting carbon nanotubes for improved efficiency and thermal stability of polymer–fullerene solar cells. Advanced Functional Materials, 2016, 26(1): 51–65

[35] Zhang L Y, Yin L W, Wang C X, et al. Origin of visible photoluminescence of ZnO quantum dots: defect-dependent and size-dependent. The Journal of Physical Chemistry C, 2010, 114 (21): 9651–9658

[36] Lai C H, Lee W F, Wu I C, et al. Highly luminescent, homogeneous ZnO nanoparticles synthesized via semiconductive polyalkyloxylthiophene template. Journal of Materials Chemistry, 2009, 19(39): 7284–7289

[37] Chien S C, Chen F C, Chung M K, et al. Self-assembled poly (ethylene glycol) buffer layers in polymer solar cells: toward superior stability and efficiency. The Journal of Physical Chemistry C, 2012, 116(1): 1354–1360

[38] Zhang S M, Guo Y L, Fan H J, et al. Low bandgap π-conjugated copolymers based on fused thiophenes and benzothiadiazole: Synthesis and structure–property relationship study. Journal of Polymer Science Part A: Polymer Chemistry, 2009, 47(20): 5498–5508

[39] Zhang Z G, Liu Y L, Yang Y, et al. Alternating copolymers of carbazole and triphenylamine with conjugated side chain attaching acceptor groups synthesis and photovoltaic application. Macromolecules, 2010, 43(22): 9376–9383

[40] Meng L, Shang Y, Li Q, et al. Dynamic Monte Carlo simulation for highly efficient polymer blend photovoltaics. The Journal of Physical Chemistry B, 2010, 114(1): 36–41

Supplementary information

As mentioned in Sections 1 and 2, the detailed experimental process in this work is as follow.

Materials and reagents

3-Thiophene methanol, 3-hexylthiophene, N-bromosuccinimide (NBS), phosphorus tribromide (PBr_3), triethylene glycol monomethyl ether, sodium hydride (NaH), *tert*-butyl magnesium chloride (*t*-BuMgCl), [1,3-bis(diphenylphosphino)propane]-dichloronickel(II), poly(3-hexylthiophene) (P3HT), zinc acetate dehydrate ($Zn(Ac)_2 \cdot 2H_2O$), potassium hydroxide, dichloromethane and 1,2-dichloro-

benzene were purchased from Sigma-Aldrich and used as received without any further purification. Tetrahydrofuran (THF) was dried over sodium/benzophenone under nitrogen and freshly distilled before use. All reactions were conducted under an atmosphere of nitrogen and all solvents used were of analytical grade, using over-dried glassware. Indium tin oxide (ITO) glass was purchased from Delta Technologies Limited and was cut into 15 mm × 15 mm. poly(3,4-ethylenedioxythiophene):poly(styrene sulfonate) (PEDOT:PSS, Baytron PA14083) was obtained from Bayer Inc.

Devices fabrication

Pre-patterned ITO-coated glass substrates (~15 Ω/sq) were cleaned by ultrasonic treatment in deionized (DI) water, ethanol, acetone, isopropyl alcohol sequentially for 15 min. After dried with clean N_2, the substrate underwent an UV-ozone treatment for 10 min. A thin buffer layer (30 nm) of filtered poly(ethylene dioxythiophene):poly(styrene sulfonate) (PEDOT:PSS) was spin coated on the top of clean ITO substrates with a speed of 4000 r/min for 30 s and then annealed at 140°C for 10 min in air to remove the moisture. The blend of P3HT/ZnO or P3HT/ZnO/P3HT-*b*-P3TEGT was spin coated on top of the PEDOT:PSS layer at a spin speed of 1000 r/min for 100 s. The thickness of the photoactive layer was typically about 150 nm. The devices were then thermal annealed at 120°C for 10 min at glove box filled by nitrogen. Finally, the LiF/Al electrode (0.8 nm/100 nm) was deposited on the active layer through thermal evaporation under vacuum. The final device structure was ITO/PEDOT:PSS/active layer/LiF/Al and the device area was defined as 4 mm^2.

Characteristics

The nuclear magnetic resonance (NMR) spectra were collected on a Bruker ARX 400 NMR spectrometer with deuterated chloroform as the solvent and tetramethylsilane (δ = 0) as the internal standard. The gel permeation chromatography (GPC) was conducted with a Breeze Waters system equipped with a Rheodyne injector, a 1515 Isocratic pump and a Waters 2414 differential refractometer using polystyrenes as the standard and tetrahydrofuran (THF) as the eluent at a flow rate of 1.0 mL/min and 40°C through a Styragel column set, Styragel HT3 and HT4 (19 mm × 300 mm, 10^3 + 10^4 Å) to separate molecular weight ranging from 10^2 to 10^6. Thermogravimetric analysis (TGA) was performed on a PerkinElmer TGA 7 for thermogravimetry at a heating rate of 20°C/min under nitrogen. Differential scanning calorimetry (DSC) was used to determine phase-transition temperatures on a Perkin-Elmer DSC 7 differential scanning calorimeter with a constant heating/cooling rate of 10°C/min. The thicknesses of each layer was measured by the spectroscopic ellipsometry (Semilab, GES5-E). Ultraviolet-visible (UV-vis) absorption spectra were measured in PerkinElmer Lambda 750 spectrophotometer. Time-resolved Fluorescence for photoluminescence (PL) decays was measured by FluoroMax-4 with a xenon lamp as the light source. Steady-state Fluorescence measurements for photoluminescence (PL) of the samples were carried on a Hitachi F-7000 PC spectrofluorophotometer. The X-ray diffraction (XRD) study of the samples was carried out on a Bruker D8 Focus X-ray diffractometer operating at 30 kV and 20 mA with a copper target (λ = 1.54 Å) and at a scanning rate of 1(°)/min. The cyclic voltammetry (CV) was performed on a CH 760 potentiostat, in an acetonitrile solution of 0.1 mol/L of ($TBAPF_6$) at a potential sweep rate of 20 mV/s at room temperature under the protection of dry N_2. A glassy carbon electrode coated with a thin film of P3HT-*b*-P3TEGT was used as the working electrode. A Pt wire and an Ag wire were used as the counter electrode and quasi-reference electrode, respectively. The electrochemical potential was calibrated against Fc/Fc^+. Atomic force microscopy (AFM) images were measured on a nanoscope III A (Digital Instruments) scanning probe microscope using the tapping mode. Transmission electron microscopy (TEM) images were recorded using a JEOL-2100F transmission electron microscope and an internal charge-coupled device (CCD) camera. Texture observations by optical microscopy were made with a Nikon E600POL optical microscope equipped with an Instec HS 400 heating and cooling stage. The samples for AFM and optical micrograph observations were prepared by spin-coating on the quartz glass at a spin speed of 1000 r/min for 100 s and the films made for TEM measurements were fabricated as if they were prepared to be active layers in photovoltaic devices. Current density–voltage (*J*–*V*) characteristics were recorded using Keithley 2400 Source Meter in the dark and under 100 mW/cm^2 simulated AM 1.5 G irradiation (Abet Solar Simulator Sun2000). All measurements were performed at room temperature under ambient atmosphere.

Synthesis of 2,5-dibromo-3-thiophenemethanol (2)

3-Thiophenemethanol (5.0 g, 4.4 × 10^{-2} mol) was dissolved in THF (40 mL) in a dried 250 mL round bottom flask wrapped in aluminum foil. The flask was degassed with argon for 15 min before being sealed under an argon atmosphere. NBS (15.6 g, 8.76 × 10^{-2} mol) was

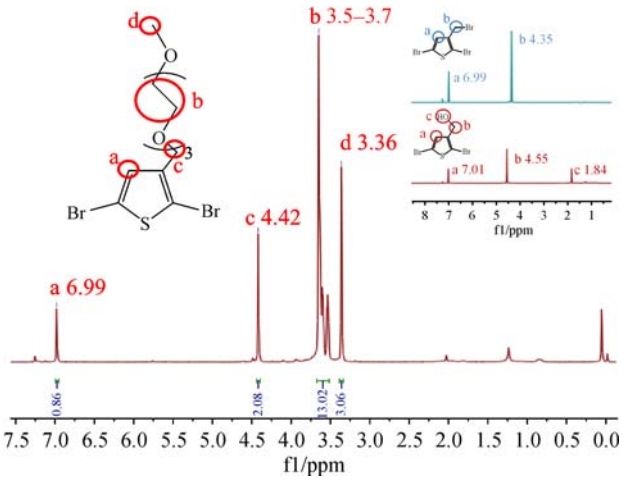

Fig. S1 ^{1}H NMR spectrum of 2,5 dibromo-3-thienyl triethylene glycol monomethyl ether (insets: ^{1}H NMR spectra of 2,5-dibromo-3-bromomethylthiophene (upper) and 2,5-dibromo-3-thiophenemethanol (below)).

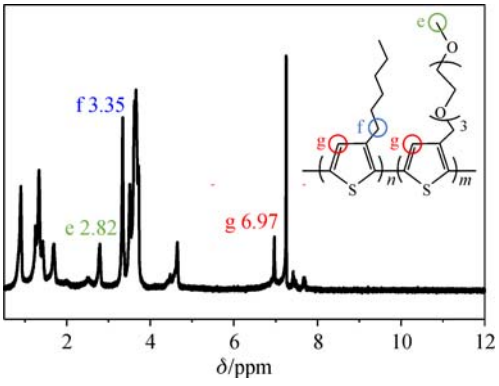

Fig. S2 ^{1}H NMR spectrum of P3HT-*b*-P3TEGT amphiphilic diblock copolymer.

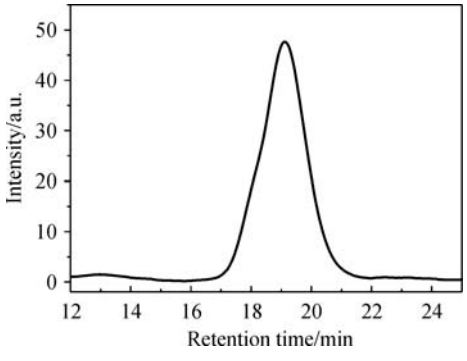

Fig. S3 Gel permeation chromatgraphy (GPC) traces of P3HT-*b*-P3TEGT amphiphilic diblock copolymers with chloroform as eluent.

added to the reaction mixture and the reaction was run at room temperature overnight. The solution was filtered to

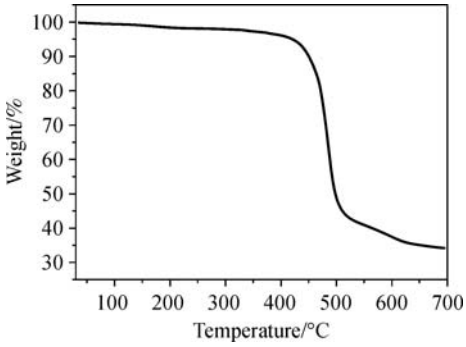

Fig. S4 The thermogravimetric analysis (TGA) of amphiphilic diblock copolymer at a heating rate of 20°C/min under a nitrogen atmosphere.

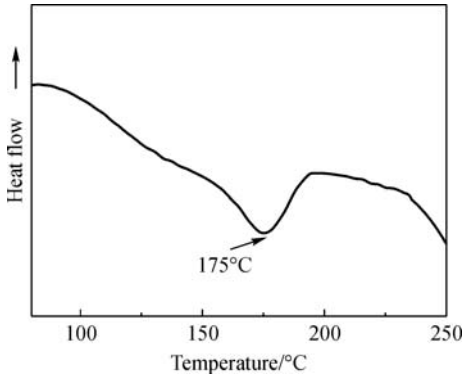

Fig. S5 Differential scanning calorimetry thermograms (DSC) of P3HT-*b*-P3TEGT.

remove residual NBS, then THF was removed by rotary evaporation. The product was dissolved in diethyl ether, then rinsed with 1 mol/L sodium hydroxide solution and water. The organic layer was concentrated and the product was eluted over silica gel using hexane:ethyl acetate (80:20). The solvent was removed by rotary evaporation to yield the desired product as an oily liquid. ^{1}H NMR ($CDCl_3$, δ, ppm): 4.60 (s, 2H) and 6.70 (s, 1H).

Synthesis of 2,5-dibromo-3-bromomethylthiophene (3)

2,5-Dibromo-3-thiophenemethanol in dry methylene chloride (100 mL) was added to a 250 mL flask, and sealed under an argon atmosphere. The flask was placed in an ice water bath and the mixture was stirred for 20 min. PBr_3 (1.73 mL, 1.84×10^{-2} mol) was added dropwise to the solution over a 15 min period. The reaction was run at room temperature for 5 h, then quenched with a 10% sodium bicarbonate solution. The organic solution was passed through a plug of Celite, rinsed with water and dried over magnesium sulfate. The solution was filtered and dried using rotary evaporation to yield the product as a light

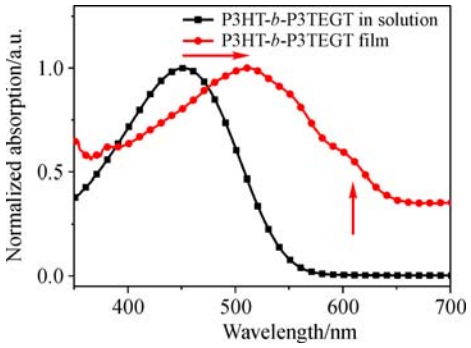

Fig. S6 UV-vis absorption spectra of P3HT-*b*-P3TEGT both in 1,2-dichlorobenzene solution and as the thin solid film.

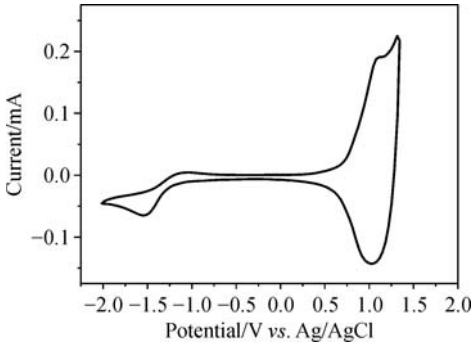

Fig. S7 Cyclic voltammograms of P3HT-*b*-P3TEGT.

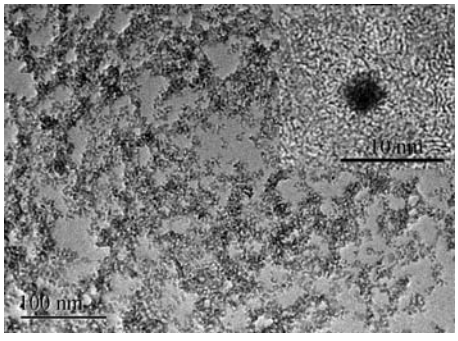

Fig. S8 TEM image of ZnO nanoparticles. The inset shows the corresponding HRTEM image.

yellow solid. ^{1}H NMR ($CDCl_3$, δ, ppm): 4.80 (s, 2H) and 6.70 (s, 2H).

Synthesis of 2,5-dibromo-3-{2-[2-(2-methoxyethoxy) ethoxy]ethoxymethyl} thiophene (4)

Triethylene glycol monomethyl ether (5.0 g, 3.0×10^{-2} mol) was dissolved in THF (125 mL) in an argon bottle and equipped with an addition funnel and septum with argon inlet. Sodium hydride (0.8 g, 3.3×10^{-2} mol) was added and after hydrogen gas evolution had ceased, the flask was sealed under an argon atmosphere. 2,5-Dibromo-3-bromomethylthiophene (9.7 g, 2.9×10^{-2} mol) was dissolved in THF (25 mL) and added dropwise to the reaction mixture at room temperature over the course of 10 min. Stirring was

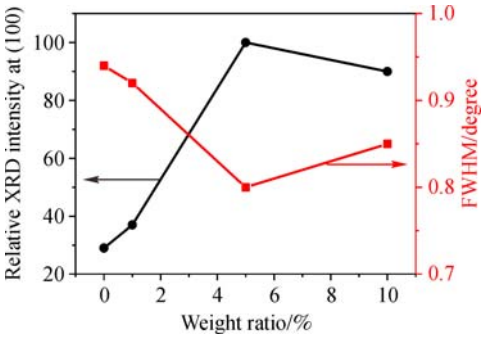

Fig. S9 Variation of XRD peak intensity and the full width at half maximum (FWHM) at (100), corresponding to the *a*-axis orientation of the P3HT crystallite, in P3HT:ZnO blend films at different P3HT-*b*-P3TEGT weight fractions.

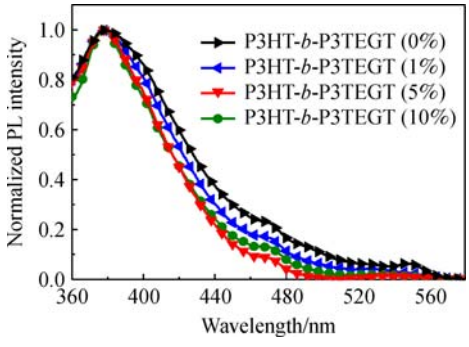

Fig. S10 PL spectra of P3HT/ZnO films blended with different amounts of P3HT-*b*-P3TEGT (λ_{ex} = 325 nm).

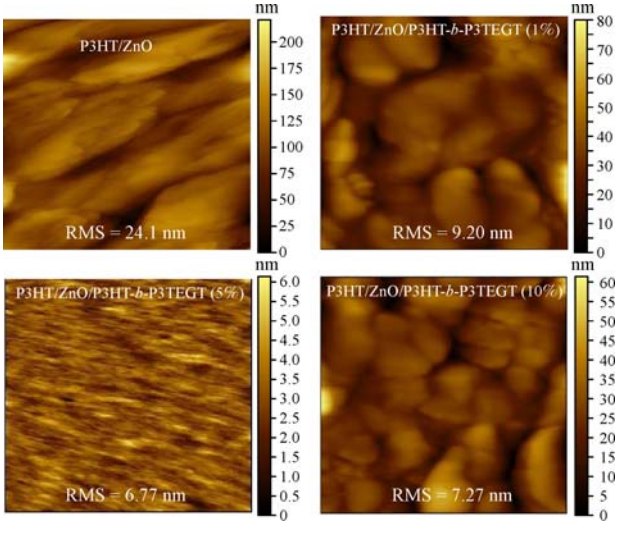

Fig. S11 AFM images of P3HT/ZnO films blended with different amounts of P3HT-*b*-P3TEGT (1 μm × 1 μm).

continued for 4 h. The mixture was run through a plug of Celite and the solvent was removed by rotary evaporation. The crude product was eluted over silica gel with a 7:3 hexane:ethyl acetate mixture. The solution was filtered and dried using rotary evaporation to yield the product as a yellow solid. ^{1}H NMR ($CDCl_3$, δ, ppm): 3.30 (s, 3H), 3.50–3.70 (m, 12H), 4.60 (s, 2H), 6.70 (s, 1H).

Synthesis of 2,5-dibromo-3-hexylthiophene (6)

3-Hexylthiophene (5.0 g, 3.0 × 10^{-2} mol) and THF (40 mL) were added to a 100 mL flask under argon atmosphere. NBS (10.6 g, 5.96 × 10^{-2} mol) was added gradually and the mixture was stirred at room temperature for 4 h. The mixture was then eluted through a plug of Celite and solvent was removed by rotary evaporation. The product was collected by distillation at 130°C as a colorless oil. ^{1}H NMR ($CDCl_3$, δ, ppm): 0.80 (t, 3H), 1.25–1.50 (m, 8H), 2.50 (t, 2H), 6.75 (s, 1H).

Synthesis of poly(3-hexylthiophene)-*block*-poly(3-triethylene glycolthiophene) (P3HT-*b*-P3TEGT) diblock copolymers

Diblock copolymer syntheses involved preparation of the Grignard derivative of each monomer and polymerization. The typical synthesis procedure of diblock copolymer was as follows: Three 2-neck round-bottomed flasks in the order were marked as A, B and C. Ni(dppp)Cl_2 catalys (24.9 mg, 4.59 × 10^{-5} mol), 2,5-dibromo-3-hexylthiophene (0.5 g, 1.53 mmol) and 2,5-dibromo-3-{2-[2-(2-methoxyethoxy)ethoxy]ethoxymethyl}thiophene (0.43 g, 1.01 mmol) were added into A, B and C, respectively. Then three flasks connected with rubber tubes were dried by heating under reduced pressure and pass through argon for removing any water and oxygen inside. After adding dry THF (5, 10 and 10 mL) into A, B and C via a syringe respectively, the solution was stirred at room temperature. 2 mol/L Solution of i-PrMgCl (0.76 mL) in THF into B via a syringe and i-PrMgCl (0.50 mL) into C a syringe, the mixture was stirred at room temperature for 1 h. Solution B was heated up to 70°C, and solution A was poured into solution B in one portion. After the reaction mixture was stirred at 70°C until atropurpureus was observed (about 5 min), solution C was also poured into solution B in one portion for overnight. The reaction mixture was precipitated into hexane. The crude polymer was filtered and purified by sequential soxhlet extractions using acetone, hexane and chloroform. The solvent was removed by evaporation to give a deep purple solid. The yielded P3HT-*b*-P3TEGT, with 1:1 weight ratio, M_n = 7700 and PDI = 2.39, was determined by gel permeation chromatography (GPC).

Synthesis of ZnO nanoparticles

The synthesis was carried out under an atmosphere of nitrogen. In a typical procedure, at first, 1.23 g of Zn-$(Ac)_2 \cdot 2H_2O$ and 55 mL of methanol were added at room

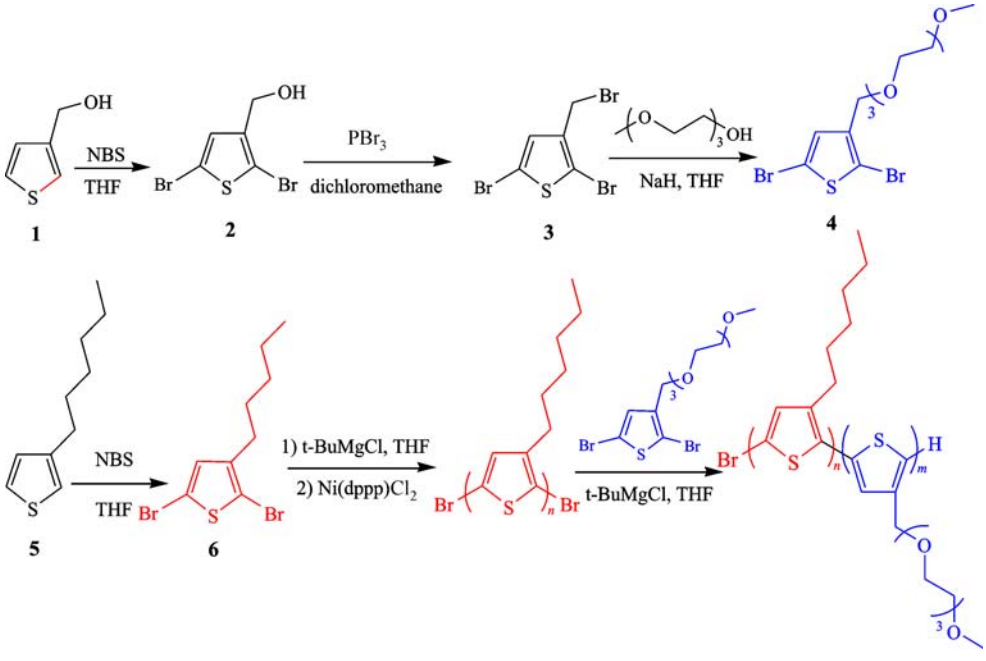

Scheme S1 Synthesis of P3HT-*b*-P3TEGT amphiphilic diblock copolymer.

temperature. Then, 25 mL of a methanol solution containing 0.48 g of KOH was added dropwise over a 20 min time interval at 60°C with vigorous magnetic stirring. After the KOH solution was added, the mixture solution was stirred at 60°C for 2 h. The product appeared as a white precipitate. After collecting by centrifugation, this white precipitate was washed with methanol for three times until it transformed to a gel-like precipitate. In detail, the washing process consisted of dispersion into methanol by sonication and subsequent centrifugation. The concentration of ZnO nanoparticles was determined by the solid residue after the evaporation of solvent, and an average ZnO concentration of 45 mg/mL had been obtained.

Preparation of P3HT/ZnO or P3HT/ZnO/P3HT-*b*-P3TEGT blends

Different ratios of P3HT-*b*-P3TEGT (0, 1, 5 and 10 wt.% with respect to the amount of P3HT, respectively) were blended into P3HT/ZnO in 1,2-dichlorobenzene to form homogeneous solutions and the weight ratio of polymer and ZnO nanoparticles was fixed at 1:2. In a typical procedure, P3HT (10 mg) or the blend (10 mg) of P3HT and a small amount of P3HT-*b*-P3TEGT was dissolved in 1,2-dichlorobenzene (556 mL), and 444 mL of ZnO solution was added. Finally, 1 mL of 1,2-dichlorobenzene solution of P3HT/ZnO or P3HT/ZnO/P3HT-*b*-P3TEGT blend was obtained.